Analyzing the Effect of the Spectral Interference of Mixed Pixels Using Hyperspectral Imagery

Shanshan Feng and Fenglei Fan

***Abstract*—The widespread presence of mixed pixels in remotely sensed images is a pressing challenge for accurate target detection and classification. Linear spectral mixture analysis (LSMA) is commonly used to address this problem by deriving remotely sensed information at the subpixel level. In the implementation of LSMA, the effects of mixed-pixel spectral interference need to be taken into account; mixed spectra would exhibit as a pure spectral characteristic when the abundance of one endmember in a mixed pixel exceeds a specific threshold. However, the thresholds of endmember abundance resulting in mixed-pixel spectral interference remain unclear. Thus, this study designed an experiment to analyze the effect of the spectral interference of mixed pixels and to identify the thresholds causing such interference by spectral similarity measures (spectral angle and spectral distance). Four types of pure endmember spectra (vegetation, high-albedo impervious surface (HIS), low-albedo impervious surface (LIS), soil) and corresponding representative mixed spectra with endmember abundances of 95%–5% at intervals of 5% were collected from Earth Observing-1 Hyperion imagery. Spectral similarity measures among the pure endmember spectra and representative mixed spectra were used to determine the thresholds of endmember abundance that cause spectral interference. The results verified the effect of the spectral interference of mixed pixels. The thresholds of abundance causing mixed-pixel spectral interference in vegetation, HIS, LIS, and soil endmembers were 70%, 75%, 80%, and 70%, respectively. Therefore, when the endmember abundance within mixed pixels exceeds the abovementioned thresholds, these mixed spectra are interfered and would exhibit as a pure spectral characteristic. Accordingly, interfered mixed pixels have to be removed before applying LSMA or other unmixing methods to avoid the effect of spectral interference.**

***Index Terms*—Endmember abundance, hyperspectral, linear spectral mixture analysis (LSMA), spectral interference, spectral similarity measure.**

I. Introduction

ALL GROUND surfaces consisting of individual pixels of remote-sensing imagery are considered spatially heterogeneous on some scale [1], [2]. Most detected land surfaces within a pixel are a mixture of more than one specific cover type, especially those from coarse- or medium-spatial-resolution imagery. Pixels with more than one distinct land cover type are regarded as "mixed pixels," while those containing only a single type are called "pure pixels" [3]. Mixed pixels extensively exist in remote-sensing imagery due to the intrinsic heterogeneous composition of ground surfaces and the coarse spatial resolution of remote-sensing sensors [4]. Therefore, it is fundamental to comprehensively understand the mixture mechanism of mixed pixels.

The widespread presence of mixed pixels is a pressing challenge for accurate target detection and imagery classification [5]–[8]. Lots of efforts have been made to address this problem for different imageries, and the linear spectral mixture analysis (LSMA) method and deep learning (DL) technique have been attracting increasing interests in previous research. For example, Hong *et al.* [9], [10] developed convolutional networks for hyperspectral image classification, showing the effectiveness and superiority of DL techniques in obtaining accurate estimation results.

The LSMA is another effective method to address the mixed-pixel problem by deriving remotely sensed information at the subpixel level. Specifically, the LSMA method assumes that the spectrum of each mixed pixel is expressed as a linear combination of the spectral signatures of the pure ground components (endmembers); this combination is then weighted by these components' corresponding areal proportions (abundance) within the pixel [11]

$$\mathrm{S}_i = \sum_{k=1}^{m} f_k S_{ik} + E\mathrm{S}_i \tag{1}$$

where $i = 1, \ldots, \mathrm{n}$ (number of spectral bands); $k = 1, \ldots, \mathrm{m}$ (number of endmembers); S_i is the spectral signature of band i; f_k is the abundance of endmember k in the mixed pixel; S_{ik} is the known spectral signature of endmember k in band i; $E\mathrm{S}_i$ is the error for band i. Because of its effectiveness in circumventing the mixed-pixel problem, LSMA has been attracting considerable interest in land cover estimation, such as impervious surface mapping [12], [13], vegetation extraction [14], [15], and snow cover assessment [16], [17].

Endmember selection plays a key role in the application of LSMA [18]. Selecting endmembers includes two basic steps: identifying the appropriate number and type of endmembers and collecting their corresponding spectral signatures. Many solutions have been used to select the appropriate number and type of endmembers (e.g., forest, grass, building, water, bare soil) for different types of remote-sensing data (multispectral

Manuscript received November 15, 2020; revised December 7, 2020; accepted December 14, 2020. Date of publication December 18, 2020; date of current version January 8, 2021. This work was supported by the National Nature Science Foundation of China under Grant 41201432. *(Corresponding author: Fenglei Fan.)*

Shanshan Feng is with the School of Geography, South China Normal University, Guangzhou 510631, China (e-mail: fengss@m.scnu.edu.cn).

Fenglei Fan is with the School of Geography, South China Normal University, Guangzhou 510631, China, and also with the Joint Laboratory of Plateau Surface Remote Sensing, Tibet University, Lhasa 850000, China (e-mail: fanfenglei@gig.ac.cn).

Digital Object Identifier 10.1109/JSTARS.2020.3045712

or hyperspectral images). In the implementation of LSMA for land cover extraction, different endmember models have been developed to estimate the areal proportions of land covers, such as the two-endmember model [19], three-endmember model (shade, nonphotosynthetic vegetation, green vegetation) [20], and four-endmember model (vegetation, impervious surface, soil, shade) [21].

The three-endmember model (vegetation, impervious surface, soil [V-I-S]) proposed by Ridd [22] received considerable critical attention for characterizing the landscape composition at the subpixel level, especially for urban landscapes. The V-I-S model assumes that the land cover in an urban structure is a linear combination of three compositions: vegetation, impervious surface, and soil; thus, it provides a guideline for decomposing urban landscapes, which is mostly selected to extract impervious surfaces [23]. Wu and Murray [24] upgraded the V-I-S model to a four-endmember model (vegetation, high-albedo impervious surface (HIS), low-albedo impervious surface (LIS), soil) based on the spectral variability of impervious surfaces; their model effectively analyzes impervious surface distributions [25]–[28].

However, the accurate abundance estimation of LSMA is usually limited by the selection of endmembers and their spectra [29], [30]. A mixed pixel is a mixture of finite endmember spectra; however, there is spectral variability in endmembers [31]. A specific endmember shows a varied spectral signature caused by differences in the illumination conditions within an image. Under these circumstances, LSMA commonly uses the typical or average spectra of pure pixels to represent the endmember spectra [30]. Such endmember variability problem would result in significant abundance estimation errors in the application of LSMA. Previous studies have shown that the spectral variability can hardly be represented by a simple LSMA model [32]. Hong *et al.* [33] proposed an augmented linear mixing model to address the spectral variability for hyperspectral unmixing, which is a positive case to effectively model the main spectral variability.

The effect of mixed-pixel spectral interference is another important factor of inaccurate abundance estimation that is often overlooked when implementing LSMA. This method assumes that all mixed spectra are linear mixtures of some set of endmember spectra and that these spectrally distinct endmembers within a pixel do not interfere with each other [34], [35]. However, this assumption is not always valid. Mixed spectra are not simply linear combinations of endmember spectra that are weighted by the abundance of each endmember within a pixel [36]. In many instances, when the abundance of one endmember within a pixel exceeds a certain threshold (dominant endmember), this mixed spectrum would exhibit as the typical spectral characteristic of the dominant endmember. That is, the dominant endmember will frequently interfere with the mixed spectra; this is called mixed-pixel spectral interference [37]. For example, in a typical urban region, mixed pixels are commonly consist of vegetation, impervious surfaces, and soil. When the abundance of vegetation endmembers within a mixed pixel exceeds a certain threshold, this mixed spectrum would exhibit as the pure spectral characteristic of the vegetation. The same situation occurs for impervious surface and soil endmembers because of the effects of mixed-pixel spectral interference.

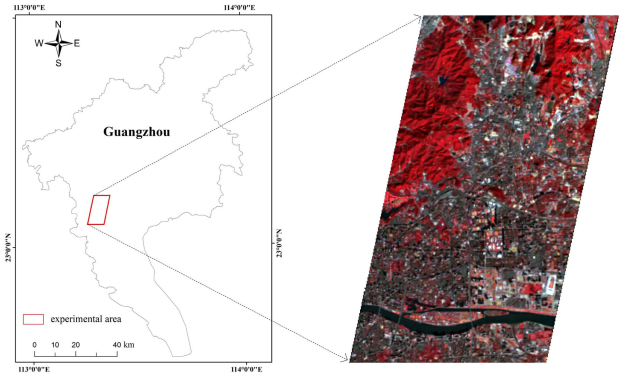

Fig. 1. Experimental area and hyperspectral image (standard false color composite image of Hyperion image, Red-Green-Blue bands corresponding to 803 nm, 650 nm, and 548 nm bands).

However, given that the specific thresholds of endmember abundance resulting in mixed-pixel spectral interference are yet to be understood, it is difficult to quantify the impact of spectral interference on mixed spectra. In this study, we design a quantitative comparative experiment to analyze the mixed spectral characteristics as the changes of endmember abundances using hyperspectral imagery. Specifically, through this experiment, two key questions are addressed: 1) How do the changes of endmember abundances affect their corresponding mixed-pixel spectral signatures? 2) What are the specific thresholds of abundances causing mixed-pixel spectral interference? The findings should offer a new understanding of mixed-pixel spectral mixtures and make an important contribution to the application of LSMA. More specifically, the effect of spectral interference in mixed pixels will be verified this study, and then the assumption of LSMA that all mixed spectra are linear mixtures needs to be redefined. Furthermore, based on specific thresholds of abundances causing mixed-pixel spectral interference, interfered mixed pixels can be identified and removed before applying LSMA, or other unmixing methods to avoid the effect of spectral interference, so as to improve unmixing accuracy to some extent.

II. Datasets and Methodology

A. Datasets and Data Processing

Experimental spectral data were collected from a one-scene hyperspectral remote-sensing image from the Earth Observing-1 (EO-1) satellite's Hyperion imaging spectrometer. A typical urban region in Guangzhou, China, was selected as the experimental area, as shown in Fig. 1. This cloud-free Hyperion image (path/row: 122/44) was acquired on December 18, 2005 and contains different land-surface materials, including impervious surfaces (sidewalks, driveways, rooftops, parking areas), vegetation, bare soil, and water bodies.

The Hyperion image contains 242 bands with a spatial resolution of 30 m. First, bands with poor data quality were removed, including those that do not have radiation calibration;

are severely influenced by water vapor and carbon dioxide; have overlapping visible (VIS), near infrared (NIR), and short-wavelength infrared ranges; or have severe band noise. A total of 153 valid bands were eventually retained, including band 9–49 (436–844 nm), band 87–120 (1037–1346 nm), band 130–165 (1447–1800 nm), and band 181–222 (1961–2375 nm). VIS wavelengths ($\leq$760 nm) and NIR wavelengths are preserved in the image. Finally, atmospheric correction was performed on the Hyperion image by the Fast Line-of-Sight Atmospheric Analysis of Spectral Hypercubes module provide by the software ENVI, which could reduce the effects of water vapor, aerosols, and other particles in the atmosphere on the reflectance properties of land surfaces. The processed Hyperion image is shown in Fig. 1.

In the collection of different types of spectral data, Google Earth imagery with a spatial resolution of 1 m was used as a reference to identify the material composition inside each pixel of the Hyperion image.

B. Design of Experiment

This experiment aims to analyze the impact of endmembers' abundance changes on their corresponding mixed-pixel spectral signatures and identify the specific thresholds of endmember abundance that cause mixed-pixel spectral interference. An urban region was regarded as an example; it consisted of three endmembers representing three typical land cover types: vegetation, impervious surface (HIS and LIS), and soil [22]. This experiment was designed to have two steps, namely, collection of spectral data and use of spectral similarity measures, to identify the threshold values causing mixed-pixel spectral interference. The overall experimental framework is shown in Fig. 2, and the process and methods are detailed in the following sections.

1) Collection of Spectral Data: Three types of pure endmember spectra (vegetation, impervious surface, soil) and a large number of representative mixed spectra were collected from the EO-1 Hyperion image. Specifically, the impervious surface can be considered to be composed of HIS (e.g., white concrete, white metal) and LIS (e.g., dim concrete, asphalt) [24].

For the four types of pure endmember spectra (vegetation, HIS, LIS, soil), the high-quality Google Earth imagery was used as a reference to select pure pixels with corresponding pure surface materials. With vegetation spectra as an example, 200 pure vegetation pixels (vegetation abundance = 100%) were selected to obtain 200 pure vegetation spectra. The pure vegetation endmember spectra were obtained from pure vegetation pixels (vegetation abundance = 100%). However, the vegetation endmember class often includes many plant species, and these can exhibit spectral variation. Finally, these 200 pure spectra were averaged to obtain one typical vegetation spectrum to represent the diverse pure vegetation spectra. The three other pure endmembers (HIS, LIS, soil) and their corresponding typical spectra were also generated from the abovementioned steps.

Mixed pixels with different abundances of the four endmembers (vegetation, HIS, LIS, soil) were collected to obtain the corresponding representative mixed spectra. With vegetation as an example, mixed pixels containing different vegetation abundances within the range of 95%–5% at intervals of 5% (vegetation abundance = 95%, 90%, …, 10%, 5%) were collected to obtain the corresponding mixed vegetation spectra. The vegetation coverage of the pixels in the EO-1 Hyperion image was manually digitized based on the corresponding Google Earth imagery using ArcGIS to obtain the representative pixels. Fig. 3 illustrates how the representative vegetation pixels were obtained by digitizing the vegetation polygons of the pixels in the EO-1 Hyperion image. In this experiment, 50 mixed pixels were selected for each interval of vegetation abundance. Then, every five pixels in each interval were used to generate an average spectrum. Ultimately, there were ten mixed spectra at each interval of vegetation abundance.

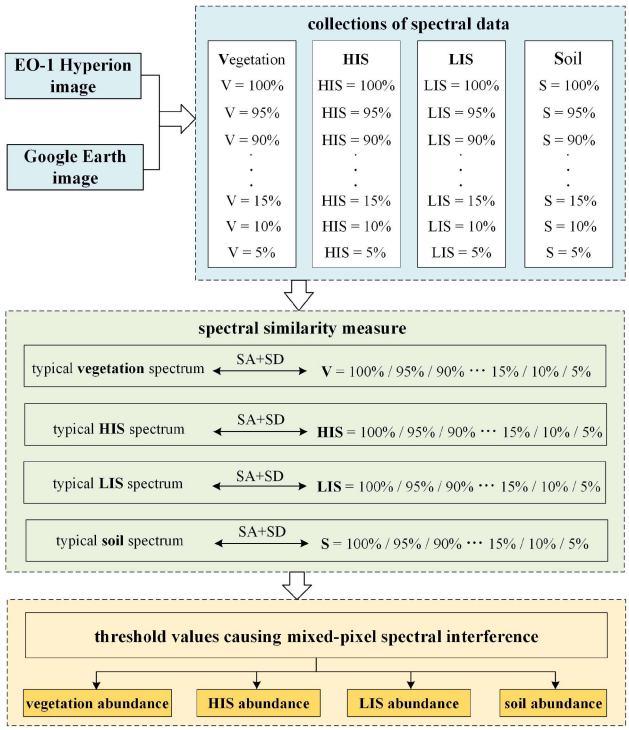

Fig. 2. Flow chart of experimental framework (V, HIS, LIS, and S represent vegetation, high albedo impervious surface, low albedo impervious surface, and soil, respectively; SA and SD represent spectral angle and spectral distance, respectively).

Representative mixed spectra with different abundances of the three other endmembers (HIS, LIS, soil) were also generated from the abovementioned steps.

2) Spectral Similarity Measure: On the basis of the pure endmember spectra and representative mixed spectra obtained in the previous step, the impact of the endmember abundance changes of mixed pixels on their spectra was analyzed. The spectral similarity among the typical endmember spectra and their corresponding representative mixed spectra were measured in this experiment. The purpose was to determine the value of abrupt change in the spectral similarity that causes a sudden change in the pure spectral characteristic. For example, spectral similarities were separately measured between the typical vegetation spectrum and the mixed vegetation spectra with abundances of 95%–5% at intervals of 5% (vegetation abundance = 95%,

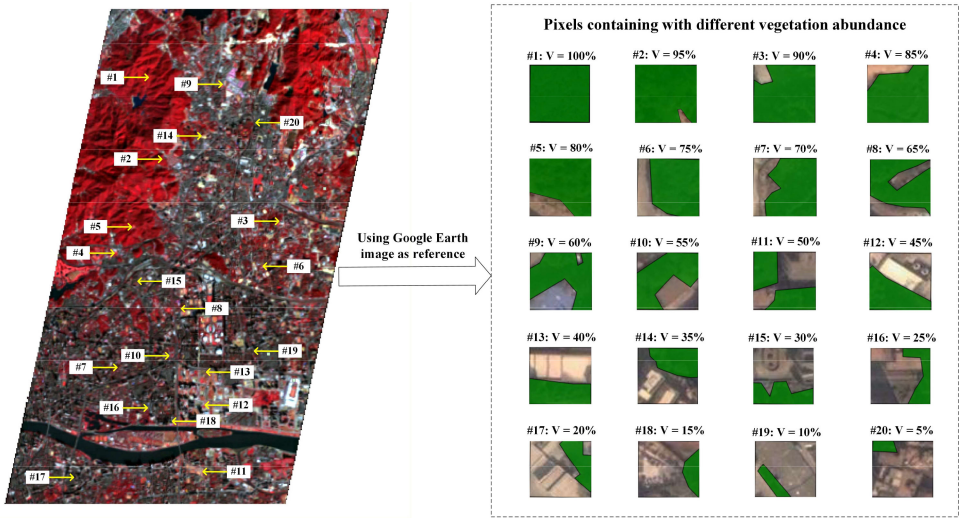

Fig. 3. Example for obtaining representative vegetation pixels by digitizing vegetation areas based on the Google Earth imagery (green polygons represent vegetation regions).

90%, …, 10%, 5%). A comparison of the spectral similarities showed that, whenever the vegetation abundance of mixed pixels exceeded a certain threshold, the spectral signatures of mixed pixels would present as typical vegetation spectra.

In addition, because of the spectral variation of pure spectra, spectral similarities between the typical vegetation spectrum (averaged pure spectrum) and 200 pure vegetation spectra (vegetation abundance = 100%) were measured. The findings would be used as references for comparison with the other spectral similarity values. Furthermore, spectral similarities between the typical vegetation spectrum and other vegetation spectra were separately measured in different spectral regions: the whole spectral range, VIS spectral range, and NIR spectral range. The spectral similarity measures of the three other endmember spectra (HIS, LIS, soil) were determined through the abovementioned steps.

Spectral angle (SA) and spectral distance (SD) measures were used to describe the spectral similarity among the endmember spectra in this experiment. These techniques are widely used in hyperspectral remote sensing [38].

a) SA measure: The SA measure determines the similarity by calculating the SA between two spectral signatures; the two spectra are treated as vectors in a space whose dimension is equal to the number of spectral bands used [39]–[41]. However, a zero SA value can be calculated, even when the two spectral vectors are not identical. This measure is insensitive to large differences in albedo or illumination effects because the SA between two vectors is independent of the spectral length of the vectors [41].

The SA between two spectral signatures (S_i and S_j) is calculated by the following formula:

$$\mathrm{SA}(S_i, S_j) = \cos^{-1}\frac{S_i \cdot S_j}{|S_i| \cdot |S_j|} = \cos^{-1}\frac{\sum_{m=1}^{n} S_{im} \cdot S_{jm}}{\sqrt{\sum_{m=1}^{n} S^2{}_{im}} \cdot \sqrt{\sum_{m=1}^{n} S^2{}_{jm}}} \quad (2)$$

where SA (S_i, S_j) is the SA between S_i and S_j; it is measured in radians and has a maximum value of 1.57 and a minimum value of 0. n is the number of bands in the image. A smaller value of SA indicates a higher similarity between the two measured spectra.

b) SD measure: The SD measure determines the similarity between two spectra by calculating the Euclidean distance between them. SD is the difference in spectral value in each waveband between two spectra. However, this measure is sensitive to the absolute magnitudes of spectra [42]. The main difference between SD and SA is that the brightness difference between the two vectors is taken into account in the SD measure, whereas the SA is invariant with brightness [43].

The SD between two spectral signatures (S_i and S_j) is calculated by the following formula:

$$\mathrm{SD}(S_i, S_j) = \sum_{m=1}^{n} |S_{im} - S_{jm}| \quad (3)$$

where SD (S_i, S_j) is the SD between S_i and S_j; n is the number of bands in the image. A smaller value of SD indicates a higher similarity between the two measured spectra.

c) Combination of SA and SD measure: In this experiment, two measure techniques, measures—SA and SD—were used to describe the spectral similarity. Take vegetation spectral similarity measures as an example. First, the SA and SD values were calculated between the typical vegetation spectrum and each pure vegetation spectrum, and these SA and SD values were separately averaged to obtain one averaged SA value and one averaged SD value. Second, the SA and SD values were calculated between the typical vegetation spectrum and every single mixed vegetation spectrum of each interval (vegetation abundance = 95%, 90%, …, 10%, 5%). Hereafter, these SA and SD values of each interval were separately averaged to generate one averaged SA value and one averaged SD value at each interval. Furthermore, the SA and SD values were calculated for

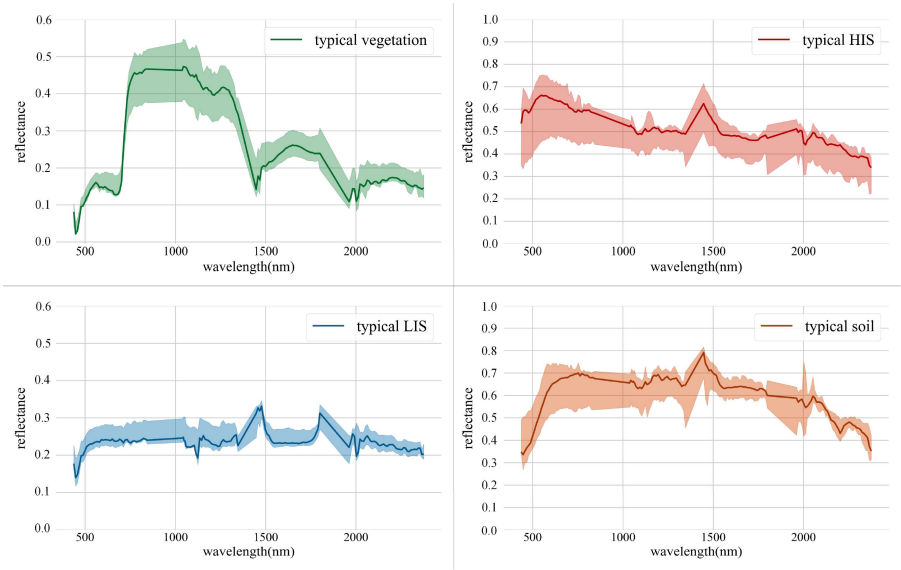

Fig. 4. Typical endmember (vegetation, HIS, LIS, and soil) spectra (the light bar represents the range of the pure endmember spectra).

the whole spectral range, VIS spectral range, and NIR spectral range.

All of the SA and SD values were, respectively, normalized in this experiment to consider them together and keep all of them in the same range: between 0 and 1. Finally, the normalized SA and SD values of each interval were added to describe the spectral similarity between the typical vegetation spectrum and the other vegetation spectra. The spectral similarity measures of the three other endmember spectra (HIS, LIS, soil) were also calculated via the abovementioned steps.

The SA and SD values were normalized with the following formula:

$$S_{\text{nor}} = \frac{S - S_{\min}}{S_{\max} - S_{\min}} \tag{4}$$

where S_{nor} is the normalized SA or SD value and ranges between 0 and 1; S is the SA or SD value of each interval; $S_{\min}$ and $S_{\max}$ are the minimum and maximum values, respectively, of all SA or SD values. Therefore, the sum of the normalized SA and SD values ($SA_{\text{nor}} + SD_{\text{nor}}$) of each interval is between 0 and 2. A smaller value indicates a higher similarity between the two measured spectra.

3) Unmixing Experiment for the Hyperspectral Image: To make the results more intuitive and convincing, an unmixing experiment for the Hyperion image was performed after determining the thresholds of endmember abundance by spectral similarity measures. The Hyperion image was unmixed by LSMA method herein. First, four pure endmember spectra (vegetation, HIS, LIS, and soil) were obtained from the abovementioned steps. Then, the image was unmixed through the LSMA method (referring to formula [1]) based on the four endmember spectra, and four estimating fraction images (vegetation, HIS, LIS, and soil) were obtain. Finally, a series of mixed pixels with estimating fraction equaling 100%, which may be interfered by the effect of spectral interference, were selected to be digitized using ArcGIS based on the Google Earth imagery.

In general, four types of pure endmember spectra (vegetation, HIS, LIS, soil) and the corresponding representative mixed spectra with endmember abundances of 95%–5% at intervals of 5% were obtained from the EO-1 Hyperion image. Moreover, spectral similarity measures (SA+SD) among the pure endmember spectra and the corresponding representative mixed spectra were used to determine the thresholds of endmember abundance that cause spectral interference. Finally, an unmixing experiment for the hyperspectral image was performed to make the results more intuitive and convincing. The results are described in the following section.

III. Result

In this study, 800 pure spectra and 760 representative mixed spectra for the four types of endmembers (vegetation, HIS, LIS, soil) were collected from the EO-1 Hyperion imagery. Each type of pure endmember spectra was averaged to obtain one typical spectrum of each endmember, as shown in Fig. 4. The spectral similarity measures between the typical endmember spectrum and the representative mixed spectra were used to analyze the mixed-pixel spectral characteristics as the abundance changes of the endmembers. The detailed results and specific thresholds are presented in the following sections.

A. Analysis of Mixed-Pixel Spectral Interference of Vegetation Endmembers

Fig. 5 displays the mixed vegetation spectra with abundances of 95%–5% at intervals of 5%. As shown in Fig. 5, the mixed vegetation spectra show as the pure vegetation spectral characteristic when the vegetation abundance is greater than or equal to 70% (V $\geqslant$ 70%). That is, when V $\geqslant$ 70%, these mixed vegetation spectra would interfere with the vegetation

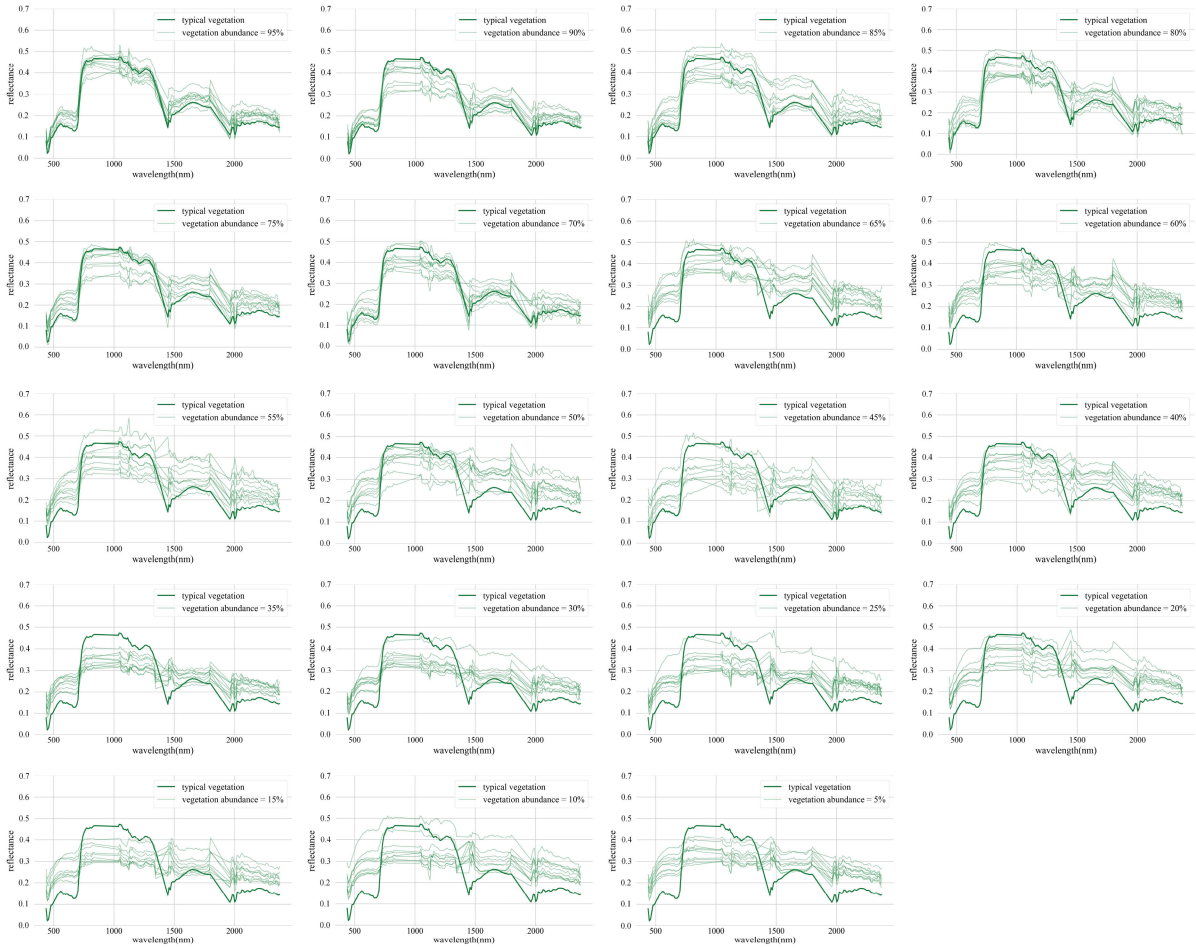

Fig. 5. Mixed vegetation spectra with abundance of 95%–5% at intervals of 5%.

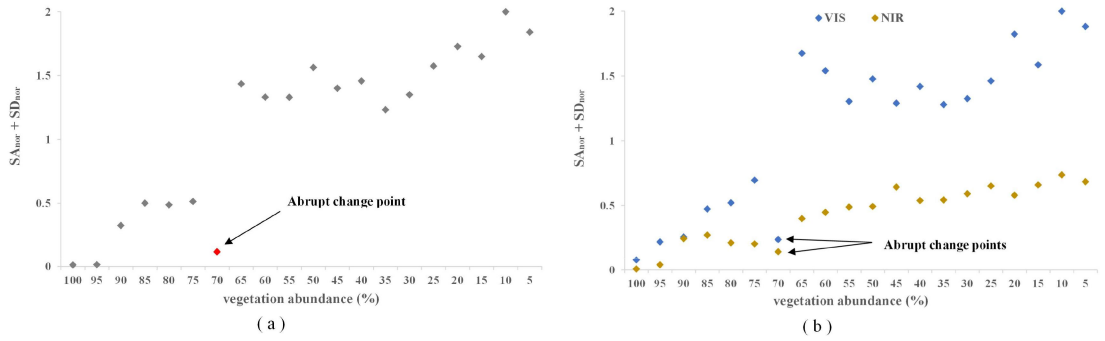

Fig. 6. Spectra similarity measures between typical vegetation spectrum and mixed vegetation spectra. (a) Whole spectral range. (b) VIS and NIR spectral range.

endmember and exhibit as pure vegetation spectra. Spectral similarity measures between the typical vegetation spectrum and the mixed vegetation spectra in the whole spectral range were calculated to further verify this phenomenon [see Fig. 6(a)]. The sum of the normalized SA and SD values ($SA_{nor} + SD_{nor}$) decreases considerably when the vegetation abundance of the mixed pixels exceeds 70%. This further confirms that the spectral similarity between the typical vegetation spectrum and the mixed vegetation spectra increases strongly when $V \geqslant 70\%$. Therefore, $V = 70\%$ is the threshold that causes the mixed-pixel spectral interference of the vegetation endmember; mixed vegetation spectra would show as a pure spectral characteristic when $V \geqslant 70\%$.

In addition, the spectral similarity between the typical vegetation spectrum and the mixed vegetation spectra was measured in both the VIS and NIR spectral ranges. The SAnor + SDnor

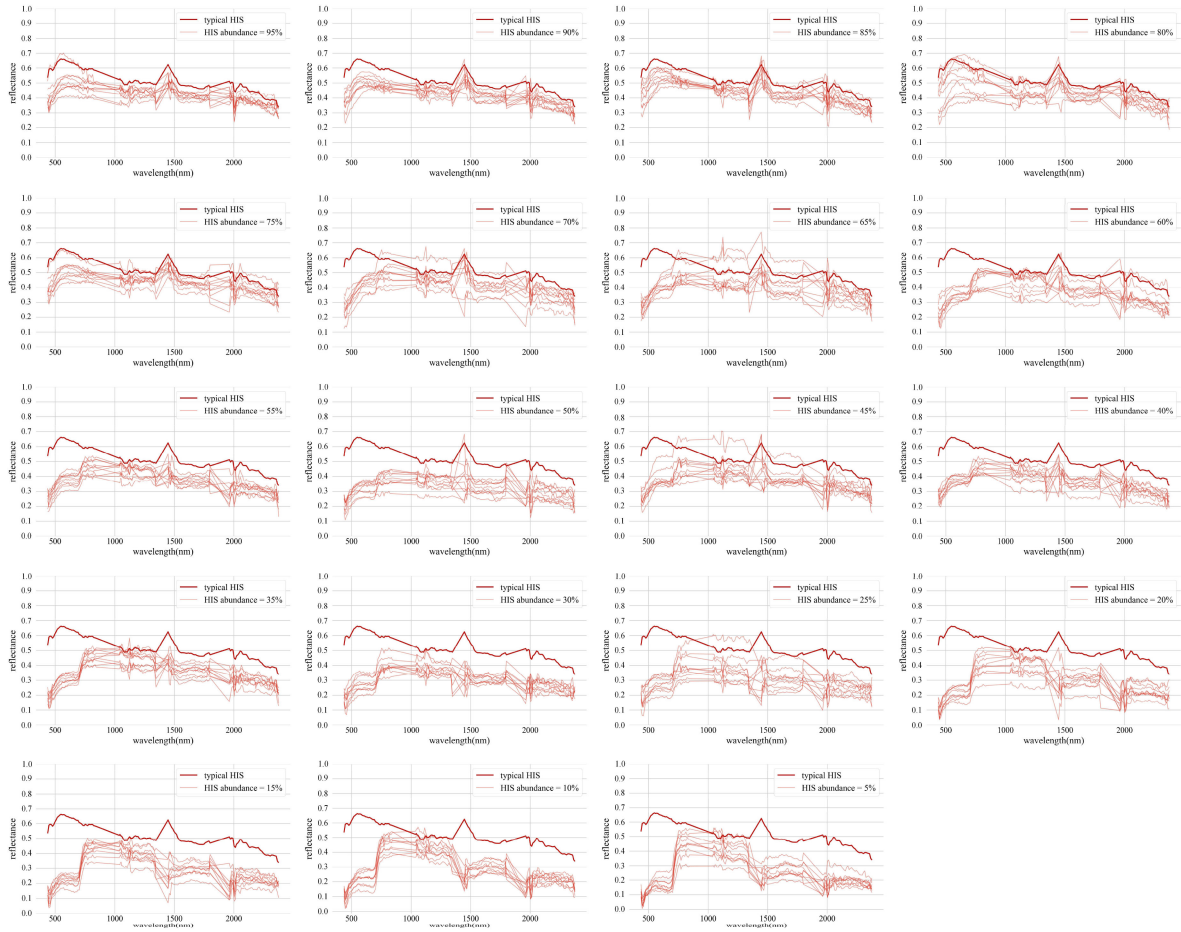

Fig. 7. Mixed HIS spectra with abundance of 95%–5% at intervals of 5%.

values were computed and are plotted in Fig. 6(b). When V $\geqslant$ 70%, the $SA_{nor} + SD_{nor}$ values both decrease considerably in the VIS and NIR spectral regions. Therefore, V = 70% is the threshold that causes the mixed-pixel spectral interference of the vegetation endmember in both spectral regions. Furthermore, the $SA_{nor} + SD_{nor}$ values in the NIR spectral region are evidently smaller than those in the VIS spectral region. Thus, the spectral characteristics in the NIR spectral region are more similar than in the VIS spectral region to those of the typical vegetation spectrum. This reveals that the mixed-pixel spectral interference of the vegetation endmember is more noticeable in the NIR spectral region.

B. Analysis of Mixed-Pixel Spectral Interference of Impervious Surface Endmembers

The impervious surface was divided into HIS and LIS. For the HIS spectra, Fig. 7 displays the mixed HIS spectra whose abundance is 95%–5% at intervals of 5%. As plotted in Fig. 7, when the HIS abundance is greater than or equal to 75% (H $\geq$75%), these mixed HIS spectra exhibit as a pure HIS spectral characteristic. The $SA_{nor} + SD_{nor}$ values among the typical HIS spectrum and the mixed HIS spectra decrease substantially when the HIS abundance of the mixed pixels exceeds 75% [see Fig. 8(a)]. Therefore, H = 75% is the threshold that causes the mixed-pixel spectral interference of the HIS endmember, and the mixed HIS spectra would exhibit as a pure HIS spectral characteristic when H $\geq$75%.

Furthermore, the $SA_{nor} + SD_{nor}$ values between the typical HIS spectrum and mixed HIS spectra were separately calculated in the VIS and NIR spectral ranges. As shown in Fig. 8(b), the $SA_{nor} + SD_{nor}$ values in the NIR spectral region are noticeably smaller than those in the VIS spectral region. The spectral characteristics in the NIR spectral region are more similar than those in the VIS spectral region to those of the typical HIS spectrum. Therefore, the mixed-pixel spectral interference of the HIS endmember is more evident in the NIR spectral region.

For the LIS spectra, Fig. 9 displays the mixed LIS spectra with abundances within the range of 95%–5% at intervals of 5%. As plotted in Fig. 9, when the LIS abundance is greater than or equal to 80% (L $\geq$80%), these mixed LIS spectra exhibit as a pure LIS spectral characteristic. The $SA_{nor} + SD_{nor}$ values between the typical LIS spectrum and the mixed LIS spectra decrease considerably when the LIS abundance of the mixed pixels exceeds 80% [see Fig. 10(a)]. Therefore, L = 80% is the threshold that causes the mixed-pixel spectral interference of the LIS endmember, and the mixed LIS spectra would exhibit as a pure LIS spectral characteristic when L $\geq$80%.

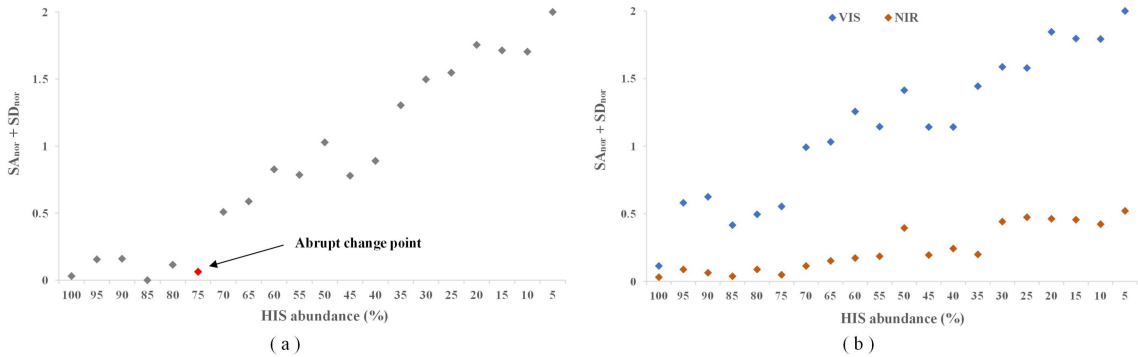

Fig. 8. Spectra similarity measures between typical HIS spectrum and mixed HIS spectra. (a) Whole spectral range. (b) VIS and near NIR spectral range.

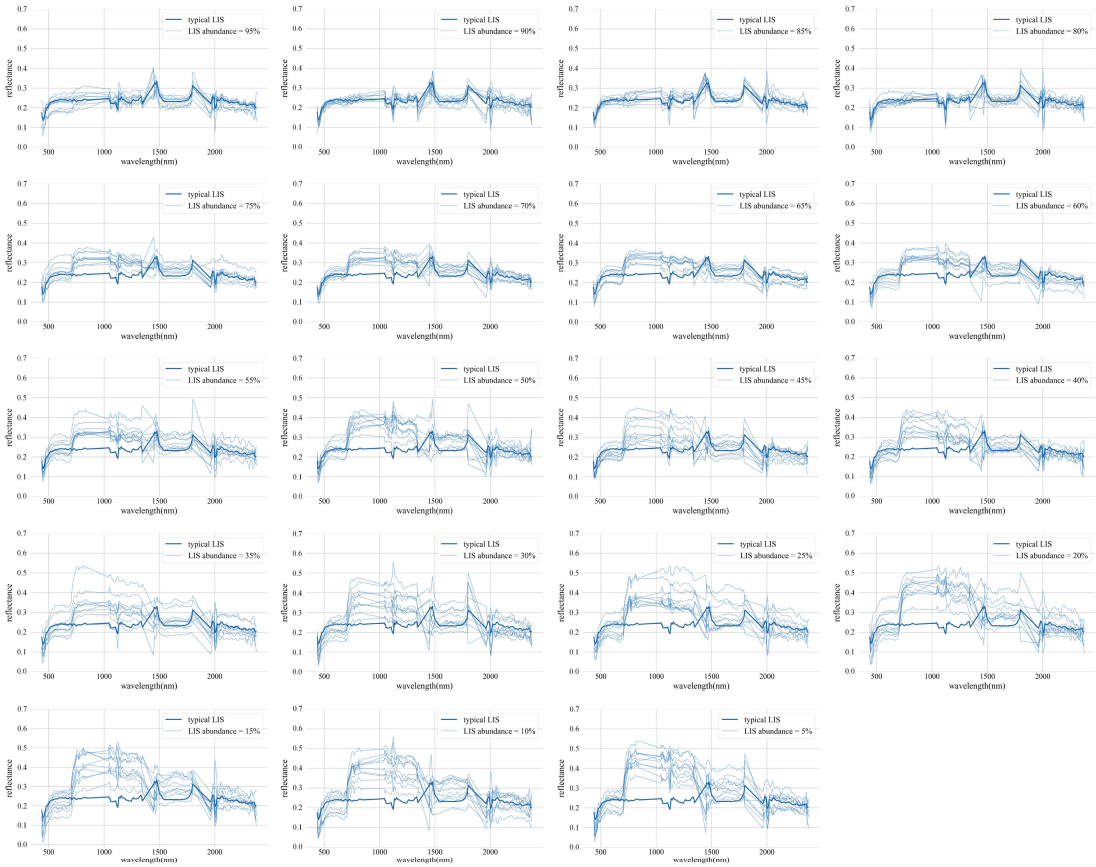

Fig. 9. Mixed HIS spectra with abundance of 95%–5% at intervals of 5%.

Moreover, the $SA_{nor} + SD_{nor}$ values between the typical LIS spectrum and the mixed LIS spectra were separately calculated in the VIS and NIR spectral ranges, as shown in Fig. 10(b). When $L \geq 80\%$, the $SA_{nor} + SD_{nor}$ values decrease substantially in both spectral regions. Therefore, $L = 80\%$ is the threshold that causes the mixed-pixel spectral interference of the LIS endmember in both spectral regions. Furthermore, the $SA_{nor} + SD_{nor}$ values in the NIR spectral region are evidently smaller than those in the VIS spectral region, which means that the spectral characteristics in the NIR spectral region are more similar than those in the VIS spectral region to those of the typical LIS spectrum. Thus, the mixed-pixel spectral interference of the LIS endmember is more noticeable in the NIR spectral region.

C. Analysis of Mixed-Pixel Spectral Interference of Soil Endmembers

Fig. 11 displays the mixed soil spectra with abundances within the range of 95%–5% at intervals of 5%. As can be seen from Fig. 10, when the soil abundance is greater than or equal to 70% (S $\geq$70%), these mixed soil spectra exhibit as

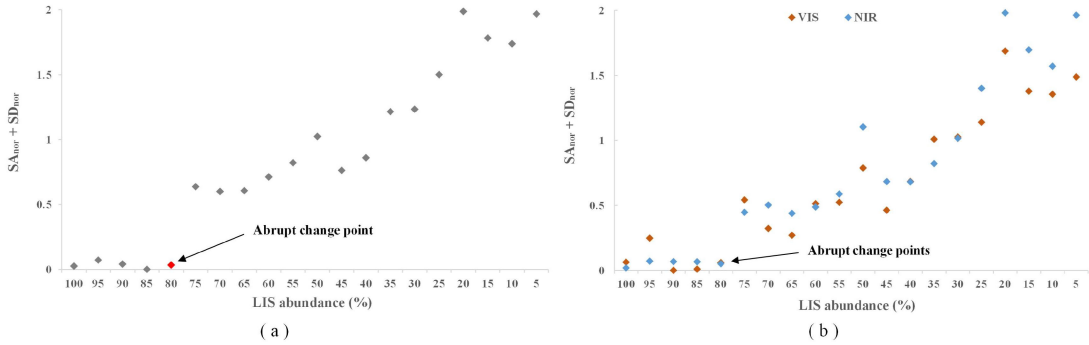

Fig. 10. Spectra similarity measures between typical LIS spectrum and mixed LIS spectra. (a) Whole spectral range. (b) VIS and NIR spectral range.

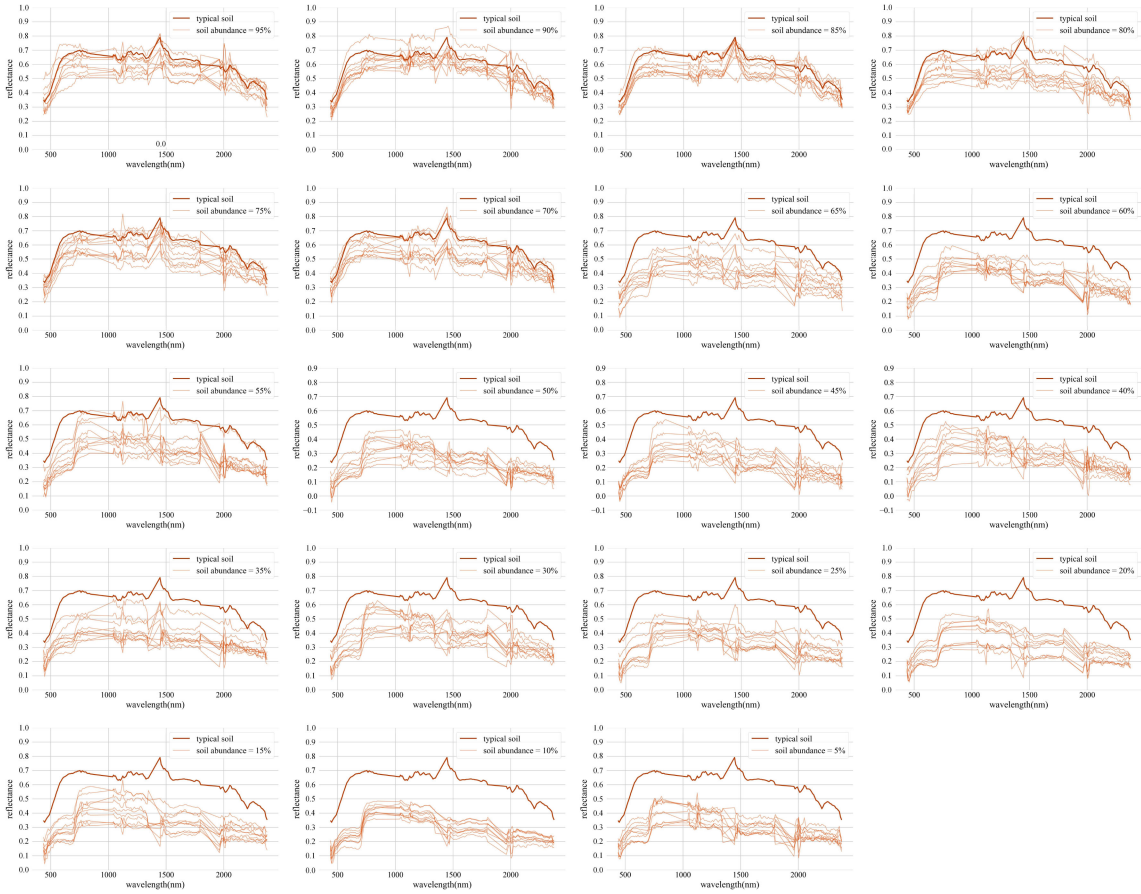

Fig. 11. Mixed soil spectra with abundance of 95%–5% at intervals of 5%.

a pure soil spectral characteristic. The $SA_{nor} + SD_{nor}$ values between the typical soil spectrum and the mixed soil spectra decrease substantially when the soil abundance of the mixed pixels exceeds 70% [see Fig. 12(a)]. Therefore, S = 70% is the threshold causing the mixed-pixel spectral interference of the soil endmember, and the mixed soil spectra would exhibit as a pure soil spectral characteristic when S ≥70%. Then, the $SA_{nor} + SD_{nor}$ values between the typical soil spectrum and the mixed soil spectra were separately calculated in the VIS and NIR spectral ranges, as shown in Fig. 12(b). When S ≥70%, the $SA_{nor} + SD_{nor}$ values both decrease significantly in both spectral regions. Therefore, L = 70% is the threshold causing the mixed-pixel spectral interference of the soil endmember in both spectral regions. Moreover, the $SA_{nor} + SD_{nor}$ values in the NIR spectral region are evidently smaller than those in the VIS spectral region, which means that the spectral characteristics in the NIR spectral region are more similar than those in the VIS spectral region to those of the typical soil spectrum. Thus, the mixed-pixel spectral interference of the soil endmember is more noticeable in the NIR spectral region.

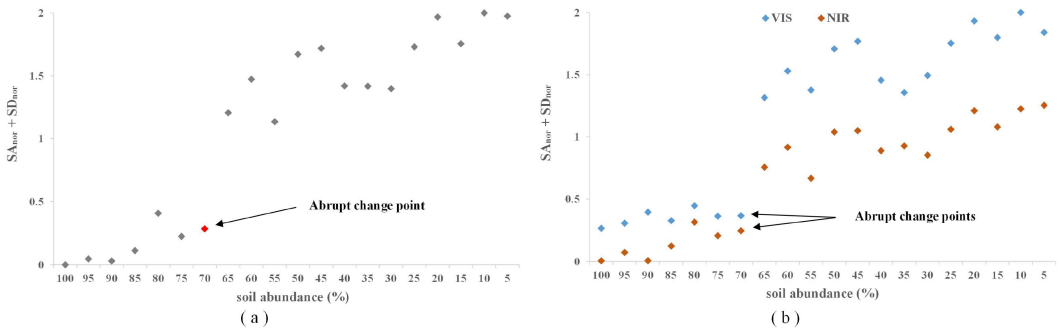

Fig. 12 Spectra similarity measures between typical soil spectrum and mixed soil spectra. (a) Whole spectral range. (b) VIS and NIR spectral range.

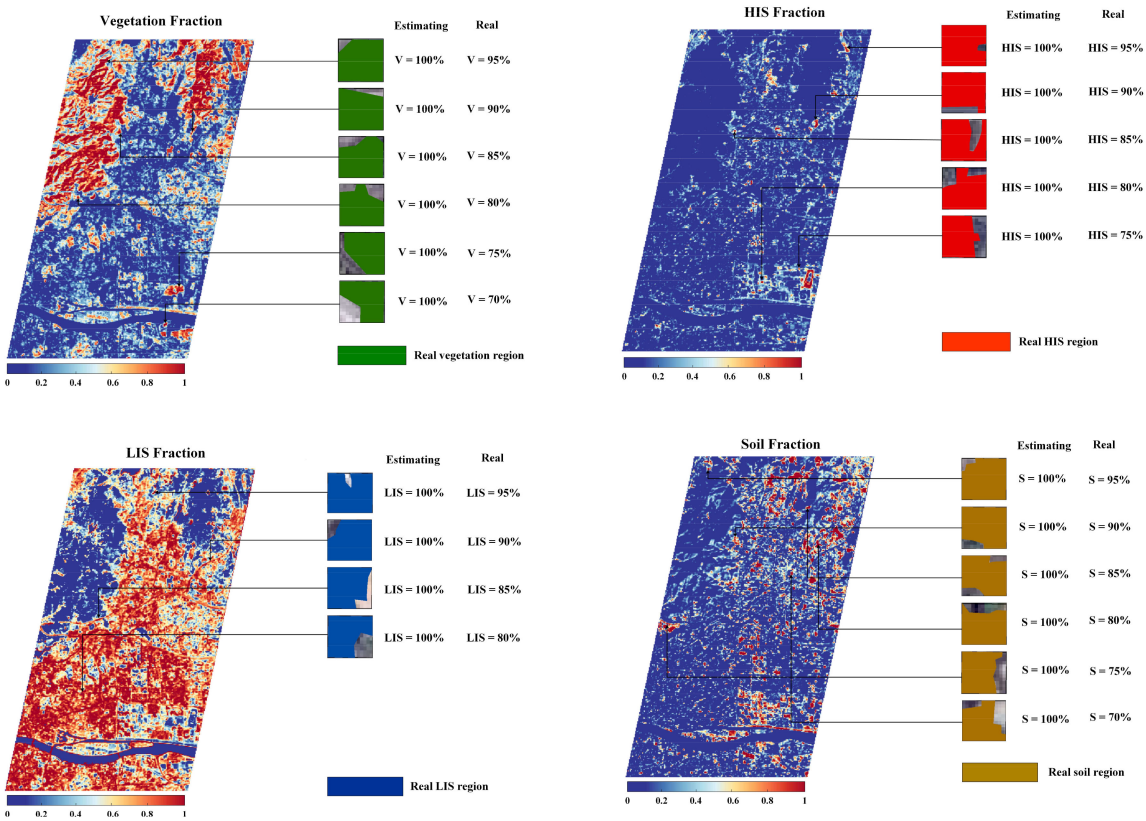

Fig. 13. Fraction images (vegetation, HIS, LIS, and soil) and examples of mixed pixels digitized real regions based on the Google Earth imagery.

D. Unmixing Results for the Hyperspectral Image

From the abovementioned results, we know that the thresholds causing the mixed-pixel spectral interference of the vegetation, HIS, LIS, and soil endmembers are 70%, 75%, 80%, and 70%, respectively. That is, when the endmember abundance within mixed pixels exceeds these specific thresholds, the mixed spectra would exhibit as pure endmember spectral characteristics. Therefore, the effects of spectral interference should be considered when applying LSMA.

To make the results more intuitive and convincing, the Hyperion image was unmixed through the LSMA method, and four estimating fraction images (vegetation, HIS, LIS, and soil) were obtained. As can be seen in Fig. 13, due to the effects of mixed-pixel spectral interference, a series of mixed pixels whose dominate endmember abundance exceeds the specific threshold were unmixed as fraction equaling 100%. Obviously, the overestimations of these mixed pixels are caused by the effects of spectral interference to some extent.

IV. Discussion

Experiments on spectral similarity measures demonstrate that mixed spectra would exhibit as pure spectral characteristics when the endmember abundance of mixed pixels exceeds specific thresholds. That is, mixed pixels are most probably affected

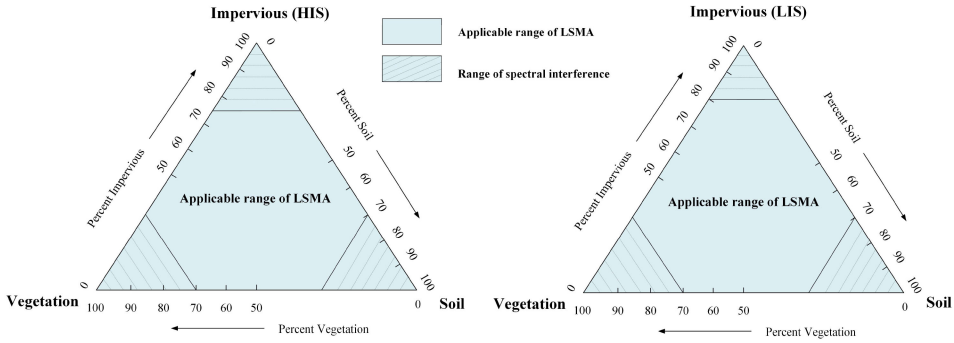

Fig. 14. Applicable range of LSMA in V-I-S model.

by spectral interference. Accordingly, changes in endmember abundance have little effect on the mixed-pixel spectral signatures when the endmember abundance exceeds the abovementioned thresholds. Consequently, the assumption of LSMA that all mixed spectra are linear mixtures of finite endmember spectra does not always hold. Over the past decades, the LSMA method has been widely applied to derive subpixel information from remote-sensing imagery; however, it does not consider the effects of nonlinear mixtures and mixed-pixel spectral interference. Mixtures of a mixed spectrum are quite complicated and may be affected by many factors. Therefore, understanding the composition mechanism of mixed spectra is an essential factor for improving the performance of LSMA.

Urban areas are mostly characterized by nonlinear mixture, as shown by case studies that observed this phenomenon [15], [44]–[49]. These studies found that nonlinear mixture effects occur in the process of remote-sensing imaging, and nonlinear mixture models can be applied to estimate the abundance of each endmember in each pixel. This study demonstrates another phenomenon of the nonlinear mixture effect, namely, mixed-pixel spectral interference, which also could not exactly meet the assumptions of LSMA. As shown by the experiment in this study, mixed-pixel spectral interference mostly occurs when the abundance of one endmember within mixed pixels exceeds the calculated hresholds. Four thresholds ($V = 70\%$, $H = 75\%$, $L = 80\%$, and $S = 70\%$) causing spectral interference of the vegetation, HIS, LIS, and soil endmembers were determined. Feng and Fan [37] also found the mixed-pixel spectral interference of vegetation endmember and identified a normalized difference vegetation index threshold value to remove these effects for accurate impervious surface mapping using LSMA. All these considerations imply that the effect of mixed-pixel spectral interference from dominant endmembers does exist in mixed pixels. When the endmember abundance of mixed pixels exceeds the abovementioned thresholds, these mixed spectra would exhibit as pure spectral characteristics. Thus, the mixtures of mixed spectra are piecewise linear representations. When the endmember abundance of mixed pixels is lower than the given thresholds, these mixed spectra become linear mixtures of their internal finite endmember spectra. On the contrary, when the endmember abundance of mixed pixels is higher than the thresholds, dominant endmembers interfere with these mixed spectra, which then exhibit as pure spectral characteristics.

Therefore, analyzing the impact of dominant endmembers on their mixed spectra is crucial for understanding mixed-pixel spectral interference and improving the implementation of LSMA. The interference of mixed-pixel spectra indicates that applications of LSMA based on the V-I-S model should have a limited range of endmember abundances within mixed pixels ($V \leq 70\%$, $H \leq 75\%$, $L \leq 80\%$, $S \leq 70\%$), as shown in Fig. 14. For example, when $V \geqslant 70\%$, these mixed spectra will interfere with the vegetation endmember, which will then exhibit as pure vegetation spectra. In the calculation of the fractional coverage of spectrally distinct endmembers using LSMA, these mixed pixels are likely to be calculated as a vegetation of 100%, even though they may contain a certain proportion of other components. This would cause the overestimation of the vegetation fraction in this situation. Accordingly, an effective suggestion can be obtained for improving unmixing accuracy. Interfered mixed pixels have to be removed before applying LSMA or other unmixing methods to avoid the effect of spectral interference.

Aside from analyzing the effect of the mixed-pixel spectral interference in different spectral regions, this study demonstrates that spectral interference is generally more evident in the NIR spectral region than in the VIS spectral region. This is because the transmittance and reflectance of NIR photons are different from those in the VIS spectral region by most surface features [14], [50]. Chen and Vierling [2] also showed that nonlinear scattering influences are extremely significant in the NIR spectral region and less influential in the VIS spectral region. For applications of LSMA, more attention should be given to mixed-pixel spectral interference in the NIR spectral region of the spectral image.

The experiment, in this study, verifies the existence of the effect of spectral interference in mixed pixels, and the specific thresholds of endmember abundance causing such interference are identified through spectral similarity measures. Although these thresholds would not be applicable to all data sources or test areas, this study demonstrates spectral interference wherein mixed spectra would exhibit as pure spectral characteristics when the endmember abundance of the mixed pixels exceeds the specific thresholds. Spectral interference should be taken

into account when applying LSMA or other unmixing methods. These findings may improve our understanding of the mixture mechanism of mixed pixels and address some limitations in LSMA and other unmixing methods.

Furthermore, representative mixed spectra with different endmember abundances were specifically selected to prove the existence of spectral interference in mixed pixels, and the thresholds causing the spectral interference of the vegetation, HIS, LIS, and soil endmembers were identified. Thus, the mixed spectra undergoing interference by the dominant endmember can be determined according to the known thresholds of endmember abundance. However, it is quite challenging to obtain the endmember types and their abundance in each pixel of remote-sensing images. Therefore, further research is required to seek an effective method of identifying the disturbed mixed pixels in practical remote-sensing imageries, such as spectral indexes.

V. Conclusion

This study confirms the existence of spectral interference in mixed pixels. Four pure endmember spectra (vegetation, HIS, LIS, soil) and a large number of representative mixed spectra collected from an EO-1 Hyperion image were used to analyze the spectral characteristics of mixed pixels as the abundance changes of endmembers by spectral similarity measures. Four thresholds (V = 70%, H = 75%, L = 80%, S = 70%) causing the spectral interference of the vegetation, HIS, LIS, and soil endmembers were determined. These indicate that, when the endmember abundance of mixed pixels exceeds the abovementioned thresholds, these mixed spectra would exhibit as pure spectral characteristics. Additionally, this study supports the fact that spectral interference is generally more evident in the NIR spectral region than in the VIS spectral region.

These findings provide a new understanding of the mixture mechanism of mixed pixels and offer useful suggestions for the implementation of LSMA and other unmixing methods. Spectral interference indicates that applications of LSMA should have a limited range of endmember abundances within mixed pixels (V $\leq$70%, H $\leq$75%, L $\leq$80%, S $\leq$70%). The disturbed mixed pixels that exceed the abovementioned thresholds need be removed before applying LSMA or other unmixing methods to avoid the effect of spectral interference, thereby improving the performance of such methods to some extent.

This study determines the thresholds of endmember abundance causing spectral interference in mixed pixels. However, calculating the areal fractions of surface features within a pixel is complex and time consuming. If the endmember abundance information of each pixel can be spectrally characterized and expressed by a spectral index, then these disturbed mixed pixels can be identified and removed easily and quickly. Therefore, effectively recognizing disturbed mixed pixels in practical remote-sensing images will be a goal for future research.

Acknowledgment

The authors would like to thank the anonymous reviewers for helping improve the manuscript.

References

[1] C. Ichoku and A. Karnieli, "A review of mixture modeling techniques for sub-pixel land cover estimation," *Remote Sens. Rev.*, vol. 13, no. 3/4, pp. 161–186, 1996.

[2] X. Chen and L. Vierling, "Spectral mixture analyses of hyperspectral data acquired using a tethered balloon," *Remote Sens. Environ.*, vol. 103, no. 3, pp. 338–350, 2006.

[3] R. E. Hyde and N. J. Vesper, "Some effects of resolution cell size on image quality," *Landsat Data Users Notes*, vol. 29, pp. 9–12, 1983.

[4] X. Chen, J. Chen, X. Jia, B. Somers, J. Wu, and P. Coppin, "A quantitative analysis of virtual endmembers' increased impact on the collinearity effect in spectral unmixing," *IEEE Trans. Geosci. Remote Sens.*, vol. 49, no. 8, pp. 2945–2956, Aug. 2011.

[5] N. Keshava and J. F. Mustard, "Spectral unmixing," *IEEE Signal Process. Mag.*, vol. 19, no. 1, pp. 44–57, Jan. 2002.

[6] D. R. Peddle and M. Smith, "Spectral mixture analysis of agricultural crops: Endmember validation and biophysical estimation in potato plots," *Int. J. Remote Sens.*, vol. 26, pp. 4959–4979, 2005.

[7] B. Somers *et al.*, "Nonlinear Hyperspectral Mixture analysis for tree cover estimates in orchards," *Remote Sens. Environ.*, vol. 113, no. 6, pp. 1183–1193, 2009.

[8] C. Shi and L. Wang, "Incorporating spatial information in spectral unmixing: A review," *Remote Sens. Environ.*, vol. 149, pp. 70–87, 2014.

[9] D. Hong, L. Gao, J. Yao, B. Zhang, A. Plaza, and J. Chanussot, "Graph convolutional networks for hyperspectral image classification[J]," *IEEE Trans. Geosci. Remote Sens.*, to be published, 2020, doi: 10.1109/TGRS.2020.3015157.

[10] D. Hong *et al.*, "More diverse means better: Multimodal deep learning meets remote-sensing imagery classification," *IEEE Trans. Geosci. Remote Sens.*, to be published, doi: 10.1109/TGRS.2020.3016820.

[11] J. B. Adams, M. O. Smith, and P. E. Johnson, "Spectral mixture modeling: A new analysis of rock and soil types at the viking lander-1 site," *J. Geophysical Res.*, vol. 91, pp. 8098–8112, 1986.

[12] C. Small, "Multitemporal analysis of urban reflectance," *Remote Sens. Environ.*, vol. 81, no. 2/3, pp. 427–442, 2002.

[13] D. Lu and Q. Weng, "Spectral mixture analysis of the urban landscape in indianapolis with landsat ETM+ Imagery," *Photogrammetric Eng. Remote Sens.*, vol. 70, no. 9, pp. 1053–1062, 2004.

[14] C. Song, "Spectral mixture analysis for subpixel vegetation fractions in the urban environment: How to incorporate endmember variability?," *Remote Sens. Environ.*, vol. 95, no. 2, pp. 248–263, 2005.

[15] B. Somers *et al.*, "Nonlinear hyperspectral mixture analysis for tree cover estimates in orchards," *Remote Sens. Environ.*, vol. 113, no. 6, pp. 1183–1193, 2009.

[16] T. H. Painter *et al.*, "The effect of grain size on spectral mixture analysis of snow-covered area from AVIRIS Data," *Remote Sens. Environ.*, vol. 65, no. 3, pp. 320–332, 1998.

[17] D. Vikhamar and R. Solberg, "Snow-cover mapping in forests by constrained linear spectral unmixing of MODIS data," *Remote Sens. Environ.*, vol. 88, no. 3, pp. 309–323, 2003.

[18] A. J. Elmore *et al.*, "Quantifying vegetation change in semiarid environments: Precision and accuracy of spectral mixture analysis and the normalized difference vegetation Index," *Remote Sens. Environ.*, vol. 73, no. 1, pp. 87–102, 2000.

[19] M. A. Theseira *et al.*, "Sensitivity of mixture modeling to endmember selection," *Int. J. Remote Sens.*, vol. 24, no. 7, pp. 1559–1575, 2003.

[20] V. C. Radeloff, D. J. Mladenoff, and M. S. Boyce, "Detecting jack pine budworm defoliation using spectral mixture analysis: Separating effects from determinants," *Remote Sens. Environ.*, vol. 69, pp. 156–169, 1999.

[21] T. Rashed *et al.*, "Revealing the anatomy of cities through spectral mixture analysis of multisepctral satellite imagery: A case study of the greater cairo region, Egypt," *Geocarto Int.*, vol. 16, pp. 5–15, 2001.

[22] M. K. Ridd, "Exploring a V-I-S (vegetation-impervious surface-soil) model for urban ecosystem analysis through remote sensing: Comparative anatomy for cities?," *Int. J. Remote Sens.*, vol. 16, no. 12, pp. 2165–2185, 1995.

[23] D. Lu *et al.*, "Methods to extract impervious surface areas from satellite images," *Int. J. Digit. Earth*, vol. 7, no. 2, pp. 93–112, 2014.

[24] C. Wu and A. T. Murray, "Estimating impervious surface distribution by spectral mixture analysis," *Remote Sens. Environ.*, vol. 84, no. 4, pp. 493–505, 2003.

[25] C. Wu, "Normalized spectral mixture analysis for monitoring urban composition using ETM+ imagery," *Remote Sens. Environ.*, vol. 93, no. 4, pp. 480–492, 2004.

[26] D. Lu and Q. Weng, "Use of impervious surface in urban land-use classification," *Remote Sens. Environ.*, vol. 102, no. 1/2, pp. 146–160, 2006.
[27] Q. Weng, X. Hu, and H. Liu, "Estimating impervious surfaces using linear spectral mixture analysis with multitemporal ASTER images," *Int. J. Remote Sens.*, vol. 30, no. 18, pp. 4807–4830, 2009.
[28] G. Li *et al.*, "Mapping impervious surface area in the brazilian amazon using landsat Imagery," *Gisci. Remote Sens.*, vol. 50, no. 2, pp. 172–183, 2013.
[29] B. Somers *et al.*, "Endmember variability in spectral mixture analysis: A review," *Remote Sens. Environ.*, vol. 115, no. 7, pp. 1603–1616, 2011.
[30] C. Zhang *et al.*, "Assessing the impact of endmember variability on linear spectral mixture analysis (LSMA) a theoretical and simulation analysis," *Remote Sens. Environ.*, vol. 235, pp. 111471–111491, 2019.
[31] C. A. Bateson, G. P. Asner, and C. A. Wessman, "Endmember bundles: A new approach to incorporating endmember variability into spectral mixture analysis," *IEEE Trans. Geosci. Remote Sens.*, vol. 38, no. 2, pp. 1083–1094, Mar. 2000.
[32] X. Fu, W. K. Ma, J. M. Bioucas-Dias, and T.-H. Chan, "Semiblind hyperspectral unmixing in the presence of spectral library mismatches," *IEEE Trans. Geosci. Remote Sens.*, vol. 54, no. 9, pp. 5171–5184, Sep. 2016.
[33] D. Hong, N. Yokoya, J. Chanussot, and X. X. Zhu, "An augmented linear mixing model to address spectral variability for hyperspectral unmixing," *IEEE Trans. Image Process.*, vol. 28, no. 4, pp. 1923–1938, Apr. 2019.
[34] J. W. Boardman, "Geometric mixture anal. Imag. spectrometry data," in *Proc. Int. Geosci. Remote Sens. Symp.*, vol. 4, 1994, pp. 2369–2371.
[35] W. He, H. Zhang, and L. Zhang, "Total variation regularized reweighted sparse nonnegative matrix factorization for hyperspectral Unmixing," *IEEE Trans. Geosci. Remote Sens.*, vol. 55, no. 7, pp. 3909–3921, Jul. 2017.
[36] W. Fan *et al.*, "Comparative study between a new nonlinear model and common linear model for analysing laboratory simulated-forest hyperspectral data," *Int. J. Remote Sens.*, vol. 30, no. 11, pp. 2951–2962, 2009.
[37] S. Feng and F. Fan, "A hierarchical extraction method of impervious surface based on NDVI thresholding integrated with multispectral and high-resolution remote sensing Imageries," *IEEE J. Sel. Topics Appl. Earth Observ. Remote Sens.*, vol. 12, no. 5, pp. 1461–1470, May 2019.
[38] M. N. Kumar, "A new hybrid spectral similarity measure for discrimination among vigna species," *Int. J. Remote Sens.*, vol. 32, no. 14, pp. 4041–4053, 2011.
[39] R. H. Yuhas, F. H. A. Goetz, and J. W. Boardmann, "Discrimination among semiarid landscape endmembers using the spectral angle mapper (SAM) algorithm," in *Proc. Summaries 3rd Annu. JPL Airborne Geosci. Workshop*, vol. 1, 1992, pp. 147–149.
[40] F. A. Kruse, "The spectral image processing system (SIPS)—Interactive visualization and analysis of imaging spectrometer data," *Remote Sens. Environ.*, vol. 44, pp. 145–163, 1993.
[41] F. A. Kruse, L. L. Richardson, and V. G. Ambrosia, "Techniques developed for geologic analysis of hyperspectral data applied to nearshore hyperspectral ocean data," in *Proc. 4th Int. Conf. Remote Sens. Mar. Coastal Environ.*, 1997.
[42] J. Chen, X. Jia, W. Yang, and B. Matsushita, "Generalization of subpixel analysis for hyperspectral data with flexibility in spectral similarity measures," *IEEE Trans. Geosci. Remote Sens.*, vol. 47, no. 7, pp. 2165–2171, Jul. 2009.
[43] F. Van der Meer, "The effectiveness of spectral similarity measures for the analysis of hyperspectral imagery," *Int. J. Appl. Earth Observ. Geoinformation*, vol. 8, no. 1, pp. 3–17, 2005.
[44] D. A. Roberts, M. O. Smith, and J. B. Adams, "Green vegetation, nonphotosynthetic vegetation, and soils in AVIRIS data," *Remote Sens. Environ.*, vol. 44, pp. 255–269, 1993.
[45] C. C. Borel and S. A. W. Gerstl, "Nonlinear spectral mixing model for vegetative and soil surfaces," *Remote Sens. Environ.*, vol. 47, no. 3, pp. 403–416, 1994.
[46] J. F. Mustard, L. Li, and G. He, "Nonlinear spectral mixture modeling of lunar multispectral data: Implications for lateral transport," *J. Geophysical Res.*, vol. 103, no. E8, pp. 19419–19425, 1998.
[47] A. Halimi, Y. Altmann, N. Dobigeon, and J.-Y. Tourneret, "Nonlinear unmixing of hyperspectral images using a generalized bilinear model," *IEEE Trans. Geosci. Remote Sens.*, vol. 49, no. 11, pp. 4153–4162, Nov. 2011.
[48] Z. Mitraka, F. D. Frate, and F. Carbone, "Nonlinear spectral unmixing of landsat imagery for urban surface cover Mapping," *IEEE J. Sel. Topics Appl. Earth Observ. Remote Sens.*, vol. 9, no. 7, pp. 3340–3350, Jul. 2016.
[49] I. Meganem, P. Déliot, X. Briottet, Y. Deville, and S. Hosseini, "Linear-quadratic mixing model for reflectances in urban environments," *IEEE Trans. Geosci. Remote Sens.*, vol. 52, no. 1, pp. 544–558, Jan. 2014.
[50] D. B. Lobell, "View angle effects on canopy reflectance and spectral mixture analysis of coniferous forests using AVIRIS," *Int. J. Remote Sens.*, vol. 23, pp. 2247–2262, 2002.

Shanshan Feng received the bachelor's degree in geographic information system from the South China Agricultural University, Guangzhou, China, in 2016. She is currently pursuing the Ph.D. degree with the School of Geography, South China Normal University. She is currently working toward the Postgraduate and Doctoral program with the School of Geography, South China Normal University.

Her major research interests include multispectral and hyperspectral remote sensing and applications in urban impervious surface mapping.

Fenglei Fan received the Ph.D. degree in environmental sciences from the Guangzhou Institute of Geochemistry, Chinese Academy of Sciences, Guangzhou, China, in 2006.

He is currently a Professor with the School of Geography, South China Normal University, Guangzhou, China. He is also the Director of Joint Laboratory of Plateau Surface Remote Sensing, Tibet University. He has been appointed as the Chair Professor of Everest Scholars, Tibet University since 2015. His major research interest includes urban remote sensing, mostly imperious surface detection using hyperspectral remote sensing.